geosciences

MDPI

Article

OH-Defects in Detrital Quartz Grains from the Julian Basin (NE Italy and Slovenia): A Fourier Transform Infrared Study

Francesco Bernardi [1,*], Henrik Skogby [2] and Davide Lenaz [1]

[1] Department of Mathematics and Geosciences, University of Trieste, 34128 Trieste, Italy; lenaz@units.it
[2] Department of Geosciences, Swedish Museum of Natural History, SE-10405 Stockholm, Sweden; henrik.skogby@nrm.se
* Correspondence: francesco.bernardi@phd.units.it

Abstract: In this study, we analyzed up to 80 detrital quartz grains from four lithic greywackes along the stratigraphic column of the Julian Basin, a synorogenic basin in the southeastern Alps between Italy and Slovenia. Fourier transform infrared spectroscopy of detrital quartz was used to investigate the sample set with interest to its OH-defect speciation and content of each associated substitution. According to several recent studies, OH-defects in quartz are correlated to petrogenetic conditions of the source material and can be used as a provenance tool. The aim of this study is to compare results based on this method with previous studies that used other methods, to better constrain the palaeogeographical reconstruction of sedimentary fluxes. Detrital quartz within the samples of the basin shows different patterns of OH-defects and water content, indicating substantial petrogenetic differences between the sediment source rocks. For the oldest analyzed sample (ca. 66 Ma), the distribution of OH-defects suggests a mixed source between igneous and non-igneous rocks, with a predominance of metamorphic material supply. Another sample (56 Ma) reveals a great variability of OH-defects and water content, indicating that the magmatic component dominates over the metamorphic component. The distribution of OH-defects in the samples at the top of the sequence (52–53 Ma) suggests an almost solely metamorphic source. These results are in line with previous studies based on heavy minerals and geochemistry.

Keywords: detrital quartz; OH-defects; Julian Basin; Italy; Slovenia

Citation: Bernardi, F.; Skogby, H.; Lenaz, D. OH-Defects in Detrital Quartz Grains from the Julian Basin (NE Italy and Slovenia): A Fourier Transform Infrared Study. *Geosciences* **2022**, *12*, 90. https://doi.org/10.3390/geosciences12020090

Academic Editors: Andrew C. Morton, Shane Tyrrell, Gustavo Zvirtes, Salvatore Critelli and Jesus Martinez-Frias

Received: 19 October 2021
Accepted: 14 February 2022
Published: 16 February 2022

1. Introduction

Clastic sediment packages are geological archives that record and preserve signatures of past geological events in source provinces. Mineralogy and petrography of sedimentary successions provide important information on the composition and role of their source rocks and, consequently, on the general paleogeography of basins. By investigating the source of sediments, we can address a wide spectrum of questions, such as sedimentation routes and mechanisms, as well as rates of sedimentation and erosion. In addition, more complex issues such as regional and global tectonic evolution can be studied by analyzing the effect these processes have on sediment provenance.

In the southeastern Alps, orogenesis, metamorphism, volcanic activity, oceanic spreading, and, of course, erosion and sedimentation are all major processes. In a framework as complex as the Alpine–Dinaric orogeny, which is still active, any improvement in knowledge is important for predicting the future modification of the landscape and its substantial effects on human activities and their planning. In addition to adding to the paleogeographic understanding of the area, provenance studies could have industrial applications including reservoir characterization and prospect for economic heavy mineral deposits.

Sedimentary provenance studies are commonly conducted on the high-density grain component, representing the detrital occurrence of essential or accessory rock-forming minerals. However, these minerals typically represent only about 1% of siliciclastic sediments

and need to be concentrated via different methods. Quartz is the second most abundant mineral of the crust and is ubiquitous in most sedimentary, metamorphic, and magmatic rocks. A quartz-based provenance method would, therefore, be widely applicable, especially as a statistically high number of analyses would be possible on individual samples. A range of studies have now been performed using OH-defect speciation as a provenance tool, with the aim of establishing a correlation between OH-defects and potential source rocks. The current paper applies this novel method to provenance studies in a sedimentary basin.

1.1. Geological Setting

The area of study is located in the northeastern Italian region of Friuli Venezia Giulia and the western part of Slovenia and embraces the southeastern portion of the Alpine arc (Carnic and Gaital Alps, Julian Alps and Prealps and Slovenian Prealps) (Figure 1).

During the Triassic period, particularly the Middle-to-Upper Triassic, almost all the area of study was covered by a shallow tropical sea with lagoons and coralline islands. In this environment, mainly carbonate platform sediments were deposited, and these are now the main rock constituent of the southern Alps, Dolomites, Classical Karst, and Dinarides [1]. Jurassic extensional activity, due to the Western Tethys opening and the beginning of the North Atlantic Rift, modified the seafloor creating a horst and graben morphology [2,3] and the Piedmont–Ligurian Ocean with the formation of oceanic crust. Carbonate platform deposition continued on the basin margins, while in the depressed zone, pelagic sediments such as micritic limestones and turbidites were deposited. The break-up of Pangea occurred in the Early Mesozoic (Triassic), causing the separation of Africa from Eurasia, and the Apulian plate was formed. Widespread Middle Triassic volcanism is associated with continental rifting in the Periadriatic region. During the Jurassic, there was an extensive seafloor spreading to the west and north of the Adria plate and, consequently, subduction of Tethys along the eastern border of the Adria promontory. By the end of the Jurassic, the Vardar Ocean formed, and in the Early and Middle Cretaceous, plate motion caused the collision of the microplate resulting in two suture zones from which the Dinarides originated. The Alpine orogeny lifted many portions of the Mesozoic seafloor carbonates. In the Late Cretaceous, subduction culminated in a continental collision of the Alpine orogenic belts that caused the creation of several foreland basins around the Alps arc, including emplacement of ophiolitic complexes. These basins collected sediment supplied from the newly uplifted areas, most of which accumulated on the continental shelf until instability led to remobilization and transport to the abyssal plains by turbidity currents. During the Eo-Alpine phase, the area of study was characterized by many foreland basins. Several basins can be recognized from NW to SE: Claut (Upper Paleocene–Lower Eocene [4]); Julian (Upper Cretaceous–Middle Eocene [5,6]); Brkini (Lower–Middle Eocene [7,8]); Istrian and Kvarner Islands (Middle–Upper Eocene [9]).

The Julian Basin (JB) is a sedimentary basin that has been active from Maastrichtian (Upper Cretaceous) to the Middle Eocene. It is placed between Italy and Slovenia and stretches from the Julian Prealps in the Bovec area to the north, to Vipavska Dolina in the south. Its eastern limit is marked by the Tolmin Mountains in Slovenia, while the southwestern border is represented by the Friuli Carbonate Platform. The basin is elongated in a NW–SE direction (Figure 1). Deposition of the turbiditic sequence was initiated during the Senonian [5] and continued until the Early Eocene [6] when molasse was deposited. The turbiditic sequence is characterized by mixed siliciclastic–carbonate material, with a total thickness of about 4000 m.

The main deposits consist of carbonate breccias, deposited in a continental slope environment. In some parts of the basin, however, several unconformities have been observed, probably due to tilting movements of slope blocks. Siliciclastic turbidites occasionally alternate with carbonate strata from the Dinaric Carbonate Platform during regression [10]. Quartz and calcite were recognized as the main constituents, plagioclases, clay minerals, and dolomites are minor components, whereas microcline and micas are very rare [4]. Clasts of dolostones, limestones, radiolarites, cherts, diabase, sandstones,

quartzites, gneisses, and low-grade schist have been recognized [4]. Among the lower Maastrichtian conglomerate outcropping in Bovec, about 60 well-sorted volcanic clasts (average diameter 0.8 cm) with tholeiitic affinities have been found [11]. These clasts show similarities with metabasites from the ophiolitic complexes of Rhodopes and Vardar zones.

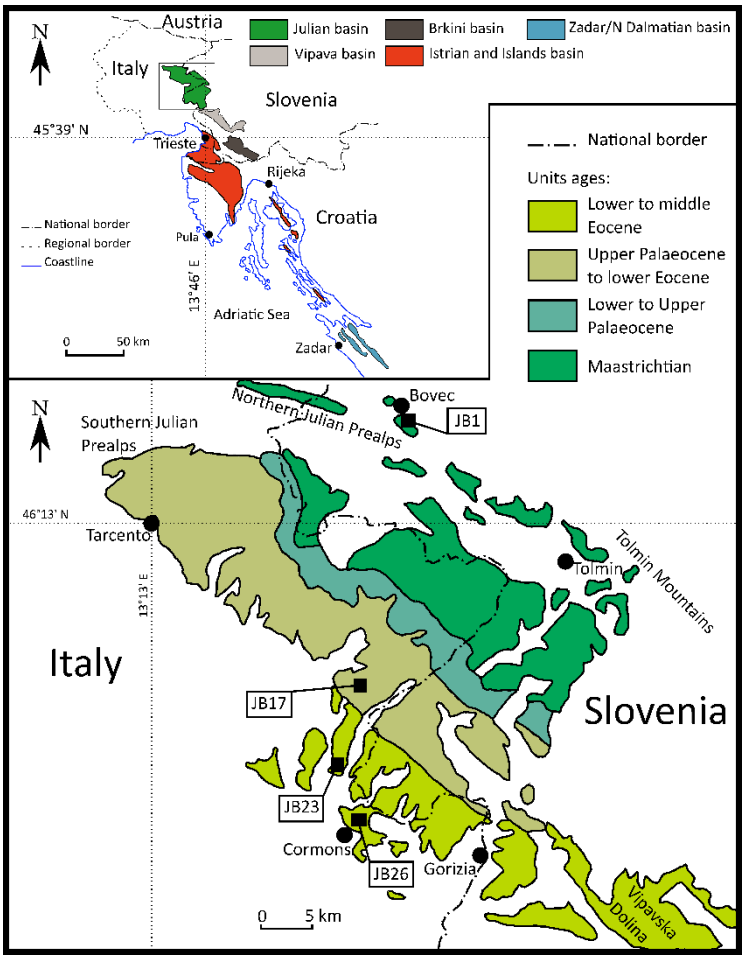

Figure 1. Flysch deposits of the SE Alps and outer Dinarides, with detail of Julian Basin and samples positions (redrawn from [12]).

1.2. Previous Studies and the OH-Defect Method

Previous mineralogical (Cr-spinel, garnet, zircon, and rutile), petrological (study of clasts in basal conglomerate and thin section analyses), and geochemical (bulk rock) studies [4,11–17] were compared with the results of this study. The results of those studies show a substantial change in source rocks during the activity of the basin. In the early stage of sedimentation, a mixed magmatic and metamorphic source has been proved. All of the studies demonstrated a momentary different input at ca. 55 Ma with an increased magmatic supply. After this paroxysmal event, the source rocks changed again, showing an almost entirely metamorphic supply.

Among the detrital components of siliciclastic rocks, quartz is highly resistant to mechanical and chemical weathering and is stable to low-grade metamorphic conditions so that it can survive erosion, transport over long distances, and diagenetic overprint. Even if considered as a nominally anhydrous mineral (NAM hereafter), quartz incorporates different amounts of hydrous defects (so-called OH-defects) during crystallization. These OH-defects can be preserved over geological time scales, at diagenetic conditions [18]. They are related to the substitution of Si^{4+} by protons and metal cations such as Al^{3+} or B^{3+}, or by $4H^{+}$, and LiOH [19,20].

The OH-defects are very strong absorbers of infrared (IR) radiation and give rise to specific absorption bands. These occur at 3595 cm^{-1} for the B-related substitution, at 3585 cm^{-1} for the $4H^+$ defect (also known as hydrogarnet substitution), and at 3480 cm^{-1} for LiOH, whereas the Al-related substitution is revealed by a triplet of peaks at wavenumbers of 3430, 3378, and 3310 cm^{-1} [21,22]. IR absorption spectroscopy can discriminate major defect types that are related to specific energies [22,23] and can also be used to quantify OH-defect concentrations at ppm levels [24,25].

Many studies have tried to find a correlation between OH-defects and the provenance of the quartz grains and a number of useful characteristics have been observed. Since the OH-defect method has been developed, it has been fundamental to understand the correlation between OH-defects and petrological conditions.

A separation between water-poor (0–5 ppm) and water-rich (>5 ppm) conditions has been suggested as a threshold to determine if quartz originates from igneous or non-igneous (both sedimentary and metamorphic) rocks [18,19]. This correlation is testified by reference materials that show, on average, lower water content for metamorphic rocks (1.5–1.6 ppm in quartzite samples), compared with igneous rocks (from 5 ppm to 16 ppm in samples of granites and rhyolites) [26].

It has been demonstrated [27] and confirmed [18,19] that quartz identified as igneous, compared with hydrothermal and metamorphic, preferentially incorporates OH as hydrogarnet—in lieu of Li-related defects. OH incorporation in quartz has been investigated at pressures between 5 kbar and 25 kbar and temperatures between 800 °C and 1000 °C. Al-related defects are coupled to mineral/melt partitioning and show a negative pressure dependence. In contrast to the Al defect, the formation of hydrogarnet substitutions appears to be positively correlated with pressure and water activity.

OH-defect speciation can be used as a monitor of igneous, sedimentary, and metamorphic processes [28]. Cold-seal pressure vessel (CSPV) experiments between 1 kbar and 3 kbar and between 650 °C and 750 °C have been performed. This experimental treatment demonstrates that Al defects are more stable during metamorphic processes than B-related and Li-related defects, and in fact, Al is dominant in quartzites and metagranites. A correlation between overall content and igneous or non-igneous source rocks and OH defect partitioning has also been demonstrated [29,30].

Recent studies of samples from fluvial and marine sediments in Japan demonstrated that very diverse and very high contents (up to 250 ppm) are likely the effects of extensional activity [20,31]. Previous studies showed that OH content in quartz can be very different (0–50 ppm [27], 0–160 ppm [18], 0–211 ppm [31], 0–65 ppm [20]).

The aim of this study was to determine and quantify the type of quartz defects in four samples in the turbiditic stratigraphic sequence of the Julian Basin. The results were compared with other provenance studies based on mineralogical, petrological, and geochemical observations. Understanding the different sources can provide information about sediment fluxes and their variation during the period of activity of the basin, providing notable data about consistency or variations in the paleogeography of the study area.

2. Materials and Methods

2.1. Sample Preparation

Four samples from the Julian Basin were selected according to their stratigraphic age: JB1 (sampled in Bovec, Slovenia) is Maastrichtian, JB17 is Upper Paleocene (from Monteaperta, Friuli Venezia Giulia region), and JB23 and JB26 are Early Eocene (from Nimis and Monte Candia, Friuli Venezia Giulia region) (Figure 2a). The rocks were crushed in a mortar; then, heavy minerals were concentrated by sieving, magnetic separation, and heavy liquids (1,1,2,2 Tetrabromoethane), for to other studies [12–16]. The residual part (mainly quartz, calcite, and feldspar) was treated with hydrochloric acid (HCl 10%) to dissolve calcite, rinsed with distilled water to remove acid traces, and dried at a temperature of 90 °C.

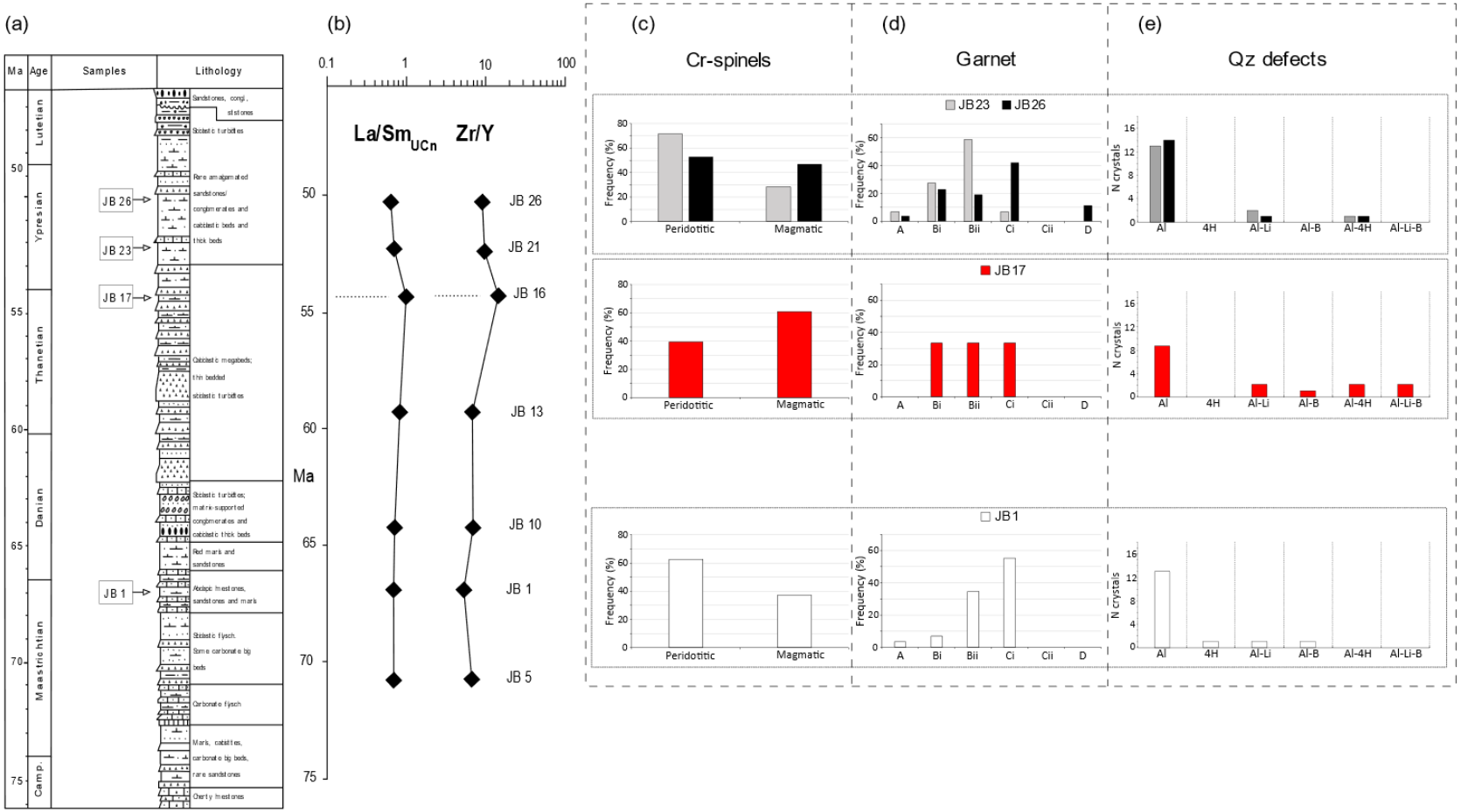

Figure 2. (**a**) Stratigraphic column of the Julian Basin ([13], modified); (**b**) stratigraphic age vs. La/Sm and Zr/Y ratios [17]; (**c**) distribution of peridotitic and magmatic Cr-spinel in JB [13]; (**d**) distribution of garnet by type in JB [14]; (**e**) type and distribution of the different OH-defects in quartz (this study). "N" denotes the number of crystals showing each defect type; samples without recognizable peaks are omitted.

For each sample, 20 quartz grains were prepared for IR spectroscopy, according to the protocol described by Stalder and Konzett [27], adding up to a total of 80 crystals. Individual quartz crystals with dimensions > 250 μm were handpicked randomly and oriented parallel to the *c*-axis in thermoplastic resin on a glass slide. Crystal alignment was checked with an optical microscope, confirmed by birefringence values of $\Delta n = 0.009$ in orthoscopic, and by "flash figures" in conoscopic illumination. Oriented crystals were manually ground and polished on both sides and maintained in the resin (except for grains JB17_003, JB17_006, and JB23_004 that were extracted from the resin). The thickness of the crystals was determined by a mechanical Mitutoyo micrometer gauge with an accuracy of ±2 μm. The crystal thicknesses vary from 63 μm to 287 μm.

2.2. FTIR Spectroscopy and Water Quantification

Polarized IR spectroscopy measurements allow the distinction between molecular water (H_2O), causing broadband between 3000 cm^{-1} and 3700 cm^{-1}, and "water" represented as OH-defects, causing sharp absorption peaks at characteristic wavenumbers between 3250 cm^{-1} and 3600 cm^{-1} [22]. It is possible to separate the OH-defect absorption bands from the H_2O absorption band, as molecular water appears isotropically (identical absorption in all crystallographic directions) and most OH-defect absorption bands are perfectly polarized perpendicular to the optical axis ($\|n_o$) [18]. The OH-defect contribution is derived by the subtraction ($n_o - n_e$) since polarized measurements $\|n_o$ record OH-defects plus molecular water, and $\|n_e$ measurements record the molecular water only. For the B-related defect, the dipole is not perfectly oriented $\|n_o$ but presents a component $\|n_e$, and to compensate for this, the intensity was calculated as $((2\ n_o + n_e)/2)$ [20,27].

IR spectra were recorded at the Swedish Museum of Natural History (Stockholm, Sweden) at room conditions, using a Bruker Vertex 70 spectrometer equipped with a halogen-lamp source and a CaF_2 beam-splitter, coupled to a Hyperion 2000 microscope with a ZnSe wire-grid polarizer and a nitrogen-cooled InSb detector. In total, 200 to 400 scans were acquired on background and sample, with a resolution of 4 cm^{-1} in the wavenumber range of 2000–7000 cm^{-1}. Two measurements ($\|n_o$ and $\|n_e$) were performed on the same spot of each crystal by turning the polarizer 90° after the first measurement. The two polarized IR spectra were subtracted, normalized to thickness, and baseline corrected by a linear baseline, within the wavenumber range of 3600–3250 cm^{-1}.

The water content determination was based on different calibrations following the Beer–Lambert law. Since IR spectroscopy is not self-calibrating, several general wavelength-dependent calibrations have been established [25,32]. These calibrations rely on hydrous minerals containing several percent of water content by weight and are based on a negative correlation between the molar absorption coefficient ε and the mean wavenumber of the corresponding OH pattern. It has been observed that these calibrations cannot be fully applied to NAMs [33] containing OH in ppm-level amount and mainly as OH-defects. To provide data for NAMs, single mineral-specific calibrations are preferable and, therefore, have been established to some extent, e.g., for the silica polymorphs [34]. In this research, defect water contents were calculated for the different substitutions (if present) using both the integrated extinction coefficient from mineral-specific calibration by Thomas et al. [34] and general wavelength-specific calibration by Libowitzky and Rossman [25].

General wavelength-dependent calibration suggests an ε based on a linear calibration curve calculated as [25]

$$\varepsilon = 246.6\ (3753 - \text{wavenumber}) \quad (1)$$

For this study, ε ranges from 38,960 L $mol^{-1}{}_{H_2O}$ cm^{-2} (for B-related defect at 3595 cm^{-1}) to 96,420 L $mol^{-1}{}_{H_2O}$ cm^{-2} (for lowest recorded Al-related defect mean peak at 3362 cm^{-1}). Mineral-specific calibration for quartz proposes an ε = 89,000 ± 15,000 L $mol^{-1}{}_{H_2O}$ cm^{-2} [34], showing that Libowitzky and Rossman [25] calibration overlaps that of Thomas et al. [34] only in the Al-related peak area (for a central peak at 3378 cm^{-1}, it gives an ε = 92,480 L $mol^{-1}{}_{H_2O}$ cm^{-2}, which falls within the 89,000 ± 15,000 L $mol^{-1}{}_{H_2O}$ cm^{-2} range). For higher values of wavenumber, the water

contents calculated with Libowitzky and Rossman [25] calibration are progressively higher, compared with the mineral-specific calibration (Table A1 in Appendix A).

Results are expressed as μg/g H_2O, which is equivalent to ppm weight H_2O notation (Table A1 in Appendix A). OH defect values were estimated to have a precision of ±10%, taking into account errors caused by background correction, thickness measurement, and crystal orientation problems [28]. In addition, there is also a systematic error based on the accuracy of the extinction coefficient, which was estimated to be ±15–20% [25,34]. The detection limit for water concentrations is strongly dependent on the spectral quality and sample thickness and estimated to vary from 0.1 ppm to 0.5 ppm for the samples studied.

Data elaboration, spectral subtraction, baseline correction, peaks integration, and water content calculation were performed using suitable analysis computer software MathWorks MATLAB® and Microsoft Excel®.

3. Results

3.1. IR Spectra

The majority of spectra show peaks that can be assigned to the typical OH-defects, but there are also spectra that do not reveal recognizable peaks (Figures 3 and 4). The Al-related defect is highly dominant, both as single occurrences and coupled with other substitutions. All the multiple substitutions contain Al coupled with one or more other defects: Al + Li, Al + B, Al + 4H, and even two grains, showing Al + Li + B defects in sample JB17 (Figure 2e). One quartz crystal from JB1 shows only a 4H defect.

3.2. Defect Water Content

3.2.1. Al-Related Defects

The Al-related substitution appears as a triplet peak at wavenumbers 3310–3378–3430 cm^{-1} (Figure 3). Within the samples analyzed, it shows a great variation in water content, from 0.4 ppm (JB26) to 107 ppm (JB17) (Table A1 in Appendix A). Quartz crystals in JB1 show a moderate variety with seven grains in the range 0–5 ppm, five grains between 5 and 10 ppm, and two grains in the range 10–15 ppm. Samples in JB23 and JB26 show similar content of Al defects (0.4–6.7 ppm). In JB23, all 16 quartz crystals show water content lower than 5 ppm, while in JB26, there is only one grain over the threshold of 5 ppm.

A clearly different behavior is revealed for sample JB17, with 11 grains under 10 ppm, one between 20 ppm and 50 ppm, and two even over 50 ppm (70 ppm and 107 ppm) (Figure 4).

3.2.2. Li-Related Defects

The Li-related substitution appears as a single peak at a wavenumber of 3480 cm^{-1} (Figure 3). Compared with Al defects, the Li-related substitutions are less abundant but still present similar patterns. Samples JB23 and JB26 show values all under 0.5 ppm. Sample JB17 presents the greatest number of substitutions and also the greatest variety, with one grain over 5 ppm (7.4 ppm). As for Al-related defects, JB23 and JB26 show very similar properties, whereas JB1 presents a relevant difference from JB23 and JB26 in terms of values. JB17 shows again a distinctly different behavior with more grains with this defect and higher water contents.

3.2.3. 4H-Related Defects

The results indicate that 4H-related defects (or hydrogarnet) appear peak centered at 3585 cm^{-1} (Figure 3); they are rare but are detected in at least one crystal for all the samples (two in JB17). Concentration values and distributions are not statistically substantial and do not show any significant patterns.

3.2.4. B-Related Defects

The B-related defects display peaks at wavenumber 3595 cm^{-1} (Figure 3) and are present only in grains from JB17 and in one grain from JB1. The absence of this substitution

in samples JB23 and JB26 reveals again the clear similarity between them. JB17 represents again a different pattern in terms of quantity and variety.

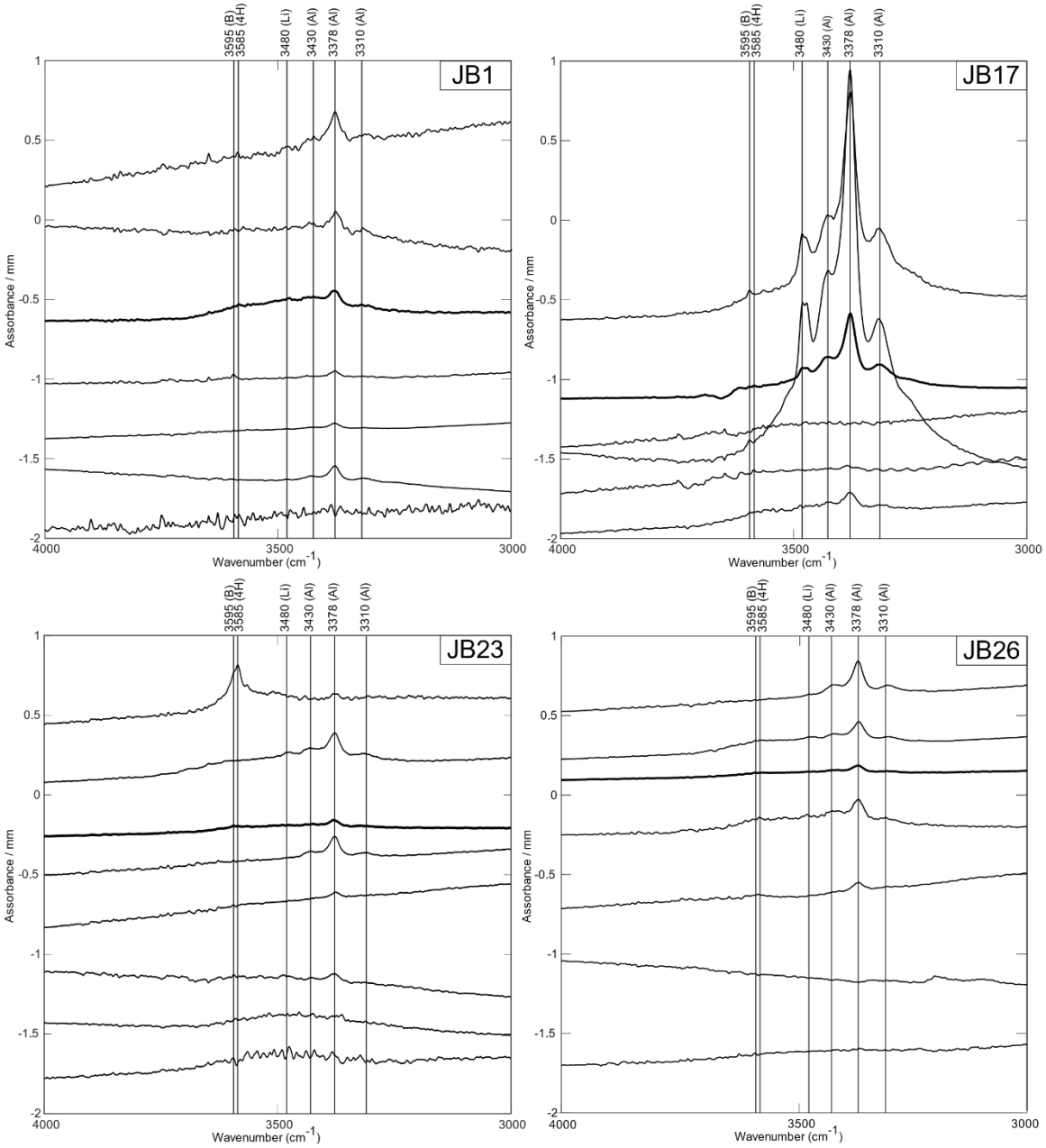

Figure 3. IR spectra ($n_o - n_e$) of representative grains, showing different noise levels and different intensities of absorbance. The spectra are offset for clarity and compared with the average spectrum for each sample (bold lines); peaks position marked with vertical lines.

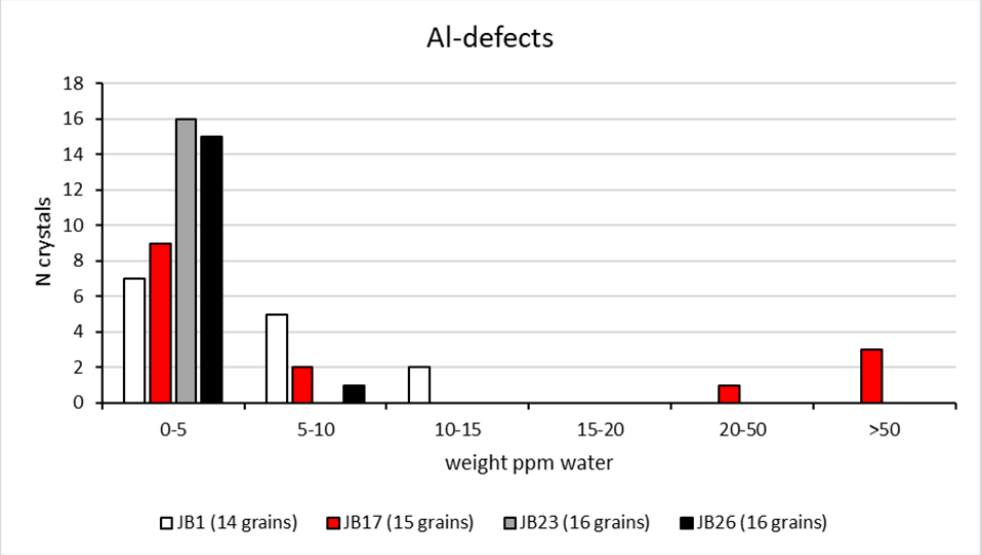

Figure 4. Quantification of the Al-related OH-defects calculated with calibration by Thomas et al. [34]. Samples without recognizable peaks are omitted.

4. Discussion

In this study, a total of 80 crystals were analyzed from four Julian Basin samples. The frequency of crystals displaying each defect is shown for comparison in Figure 2e. The total amount of OH is in the range 0–15 ppm for JB1, 0–112 ppm for JB17, 0–4.4 ppm for JB23, and 0–6.7 ppm for JB26.

Sample JB1 is the oldest in the stratigraphic column (ca. 66 Ma). The grains from this sample show moderate variability in defects, with an abundance of single Al-related defects and only a few of the other types. The water content for Al defects spans from 1.2 ppm to 15 ppm. Other defects are present in only one grain each, with the water contents of Li: 1.3 ppm, 4H: 1.3 ppm, and B: 0.3 ppm. The observations suggest that both metamorphic and non-metamorphic sources are present [18,27], with metamorphic rocks prevalent.

Samples JB23 and JB26 are the youngest in the stratigraphic column and are almost coeval (between 52 Ma and 53 Ma). These two samples display very similar behaviors, with a great number of grains bearing Al defects but corresponding to low water contents, for JB23, between 0.4 ppm and 4.4 ppm, and for JB26, between 0.4 ppm and 6.7 ppm. Li-related substitutions are in the range of 0.1–0.3 ppm, in grains from JB23, and 0.1 ppm in the only grain in JB26. There are no B-related substitutions. An almost solely metamorphic origin can be suggested for these samples, according to the above-mentioned correlations [18,27].

Sample JB17 is slightly older than JB23 and JB2, but considerably younger than JB1, with an age of about 56 Ma. The spectra of the grains from this sample show different patterns to those of the others, both in terms of defect variability and the corresponding water contents. In this sample, almost half of the grains show defects with multiple substitutions (Al + Li, Al + B, Al + 4H, Al + Li + B) (Figure 2e), with very high values of water content, especially for the Al-related defect (0.8–107 ppm, Figure 4). The Li-related defect shows high variability and the highest content within the basin (0.9–7.4 ppm), and the same is observed for B (0.1–0.3 ppm), which also shows the highest values. The 4H defect shows no great variability and average content (0.1–0.5 ppm). The great number of Al- and Li-related defects, and their notable variability, suggests the presence of a mainly volcanic source, possibly even late-stage volcanic (hydrothermal Li defect [20]) source material. The presence of 4H defects indicates that there is also a supply from high-pressure rocks. This is the only sample in which volcanic quartz is almost in the same percentage as metamorphic.

In order to determine the source rocks of the detrital quartz, we need to consider the previous studies on the Julian Basin.

Cr-spinel chemistry indicates they were derived from the Dinarides [13,16]. Based on the Fe^{2+}/Fe^{3+} and TiO_2 content of Cr spinels, it is possible to discriminate between peridotitic (or restitic spinels) and magmatic (crystallized from percolating melts within the peridotites) [13,35]. These parameters show that, for samples JB1, JB23, and JB26, more than 60% of the Cr-spinels are peridotitic, while in JB16 (stratigraphically close to JB17 studied here) they represent only 40% of the Cr spinels (Figure 2c).

Within the peridotitic spinels, there is a widespread distribution for JB1 and JB17, while they are concentrated within the 50–70 Cr# interval for the two Eocene samples (JB23 and JB26). The magmatic spinels show a clear shift to low Cr# values (<40) in JB17 and JB23 samples. The chemistry of the volcanic spinels demonstrates that at least four different source areas were present in the area including (1) MORB or MORB-type back-arc rocks that are mainly present in JB16, (2) subduction-related back-arc and continental rifting, (3) plume-related intraplate basalts, and (4) island arc tholeiites or boninites [13,16].

The main spinel detritus in the Julian Basin derived from the suprasubduction zone of the Vardar Ocean during the beginning of deposition in the Maastrichtian [36]. These supplies continued during the Paleocene, when MORB-type spinels from the spreading ridge of the Pindos Ocean arrived as well. Successively, a new input of suprasubduction zone detritus arrived during the Early Eocene times, possibly related to intra-oceanic subduction of the Pindos Ocean. It is interesting to note that the Vardar and Pindos areas are divided by the Drina–Ivanica microcontinent.

Recently, trace and rare earth (RE) elements in garnets have been studied from the region [14]. The authors analyzed about 250 garnets from different basins in the SE Alps, including in the Julian Basin, where the most common types are, according to Mange and Morton [37] classification, Bi, Bii, and Ci, with very low amounts of A and D. Almost 90% of garnets from JB1 belong to the Bii and Ci types, almost 85% of garnets from JB23 are in the B typology, JB26 shows a wider spread distribution (including D type), while JB17 present contributions that are equally distributed between the Bi, Bii and Ci types (Figure 2d). Even if the authors did not link the supplies to specific sources, it is possible to suppose that the Ci-type garnets were supplied from the suprasubduction zone (SSZ) of the Vardar ophiolites and their metamorphic soles. The presence of garnets related to granitoids and metasediments (B-type garnets are related to amphibolite facies metasediments [37]) possibly involves contributions from different ophiolitic sources but also from the Drina–Ivanica terrane. Upper Jurassic granitoid rocks associated with the East Vardar ophiolites form a discontinuous belt from Serbia in the north to northern Greece in the south. Two groups of intraophiolitic granitoids are distinguished: (1) diorite, quartz diorite, and quartz monzodiorite; (2) two subgroups of granites and granodiorites [38]. However, none of these granitoids is garnet bearing.

Detrital amphiboles (actinolite, Mg-hornblende, barroisite, and glaucophane) associated with pyroxenes have been found in Lower Eocene (about 52 Ma) turbidites of the Julian Basin [15]. These samples are stratigraphically located between JB23 and JB26. Actinolite and Mg-hornblende are derived from low-to-medium-grade metamorphic rocks (metavolcanics in greenschist facies). Barroisite is the ultra-high-pressure type of calcic amphibole, and it is considered a marker of retrogressive metamorphism. Glaucophane is representative of high-pressure blueschist facies metamorphic rocks. Omphacites are related to subsolidus recrystallization of basic igneous rocks at high-pressure and temperature in eclogite facies. The occurrences of these minerals are commonly related to the erosion of high-pressure-low-temperature metavolcanics in green-blue schist and eclogitic facies. According to the low amount and distribution of these minerals, it has been suggested that they belong to limited metamorphic bodies exhumed at about 56 Ma during a phase of uplift of the Dinarides [15,39].

As regards the geochemistry of the basinal sediments, the oceanic source of sediments at 56 Ma (sample JB16) is confirmed by De Min et al. [17]. There are different parameters that can be used to prove the source of the sediments. The Cr/V ratio reveals that sample JB16 (Cr/V = 33.22) has a non-peridotitic source (that spans between 2 and 20). Additionally,

the study of trace and RE elements can provide further information about the source of the sediments. Variation in chemical ratios within the stratigraphic column of Julian Basin display this difference. In fact, considering Zr/Y and $(La/Sm)_{UCn}$, it is clear that the greater variation corresponds to sample JB16. This variation seems to demonstrate the paroxysmal moment of the Dinaric orogenesis [17] (Figure 2b).

The present study shows that the detrital quartz crystals in the Julian Basin show different patterns of defects and different water contents, suggesting differences in sediment source. There is a change from the bottom of the stratigraphic sequence, where a mixed igneous and non-igneous source is present, and the top, where an almost solely metamorphic rock type source occurs. As observed for other mineral systematics, quartz from sample JB17 show the greatest variability in supplies. The abundance and heterogeneity in the types of defects, the water content (up to over 100 ppm for Al related, and from 0.9 ppm to 7.4 ppm for Li related), and their great variability suggest a more complex source for the sediments, with the magmatic component dominant over the metamorphic component. These features confirm the distinctive provenance in this part of the sequence, in line with previous studies (Figure 5).

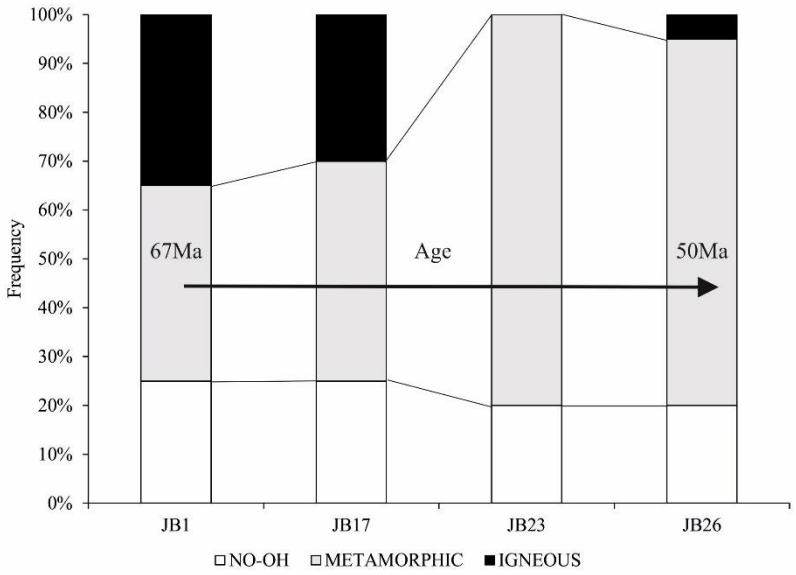

Figure 5. Frequencies of quartz grains from igneous and non-igneous sources from 67 Ma to 50 Ma. As igneous quartz, we considered all grains with OH > 5 ppm according to [18,19].

According to the previous interpretations [13,14,36], it is possible that the main volcanic detrital quartz could be supplied from the Drina–Ivanica microcontinent or the intraophiolitic Jurassic granitoids, while the metamorphic quartz is related to the metamorphic soles of ophiolitic emplacement related to the closure of the Vardar (JB1 and JB17) and Pindos oceans (JB23 and JB26), respectively.

New studies are currently ongoing with more samples, in order to verify if there was a paroxysmal event at about 56 Ma (JB71), or if the change in quartz supplies starts between the beginning of deposition at 67 Ma (JB1) and JB17. Chemical analyses on the same grains will add more constraints to the genesis of the quartz crystals. The most common trace elements in magmatic quartz are Al, Li, and Ti, with medians of 447, 39.6, and 17.4 ppm in S-type rare-metal granites, and 160, 15, and 6.6 ppm in A-type rare-metal granites [40]. It is possible that the coupling of OH-defect data with the trace element content of quartz will better discriminate granitoid sources.

5. Conclusions

This research demonstrated that the OH-defect method is a powerful tool for provenance analysis. Quartz is extremely abundant in siliciclastic rocks, easy to recognize, and

does not need to be concentrated. As already stated, the preparation of single crystals is relatively easy, and the acquisition of spectra is also fast and simple. Moreover, the analyses are not very expensive. This means that provenance studies would be easily enhanced from this type of study. Although heavy minerals provide unique opportunities to clearly establish supply from certain rocks where they are rock-forming or accessory minerals, quartz is almost ubiquitous and much more abundant. Acquisition of provenance data from quartz will, therefore, increase the chances of identifying all possible sources of the studied sediments and thereby improve palaeogeographical understanding. Many other studies of provenance and possible source lithologies based on this method will surely follow.

Author Contributions: Conceptualization, F.B. and D.L.; methodology, F.B. and H.S.; formal analysis, F.B.; investigation, F.B., H.S. and D.L.; writing—original draft preparation, F.B., H.S. and D.L.; writing—review and editing, F.B., H.S. and D.L.; supervision, H.S. and D.L. All authors have read and agreed to the published version of the manuscript.

Funding: This research received no external funding.

Data Availability Statement: Not applicable.

Acknowledgments: Carita Augustsson and an anonymous reviewer are kindly acknowledged for their helpful comments that significantly improved the clarity of the manuscript. Andrew Morton is kindly acknowledged for text revision and English improvement. F.B. wants to thank the University of Trieste extra Erasmus international mobility program for financial support.

Conflicts of Interest: The authors declare no conflict of interest.

Appendix A

Table A1. Water content for samples calculated with Thomas et al. [34] (shaded column) and Libowitzky and Rossman [25] calibrations. ND means that no recognizable spectra were detected.

Sample	Thickness	Wavenumber	Absorption Integration	Density	ε	H_2O ppm [34]	ε	H_2O ppm [25]	Defect
JB1_001	215	3375	1.44	2.65	89,000	5.1	93,220	4.9	**Al**
JB1_002	230	ND	ND	2.65	89,000	ND	ND	ND	**-**
JB1_003	260	ND	ND	2.65	89,000	ND	ND	ND	**-**
JB1_004	276	ND	ND	2.65	89,000	ND	ND	ND	**-**
JB1_005	144	3585	0.25	2.65	89,000	1.3	41,430	2.9	**4H+**
JB1_006	171	3370	0.56	2.65	89,000	2.5	94,450	2.4	**Al**
JB1_007	147	3371	2.81	2.65	89,000	15	94,200	14	**Al**
JB1_008	175	3368	0.49	2.65	89,000	2.1	94,940	2.0	**Al**
JB1_009	181	3369	1.34	2.65	89,000	5.7	94,690	5.3	**Al**
JB1_010	146	ND	ND	2.65	89,000	ND	ND	ND	**-**
JB1_011	254	3380	0.41	2.65	89,000	1.2	91,980	1.2	**Al**
JB1_012	73	3379	0.60	2.65	89,000	6.3	92,230	6.1	**Al**
JB1_013	179	ND	ND	2.65	89,000	ND	ND	ND	**-**
JB1_014	153	3374	1.66	2.65	89,000	8.3	93,460	7.9	**Al**
JB1_015	63	3370	0.52	2.65	89,000	6.3	94,450	5.9	**Al**
JB1_016	128	3368	1.89	2.65	89,000	11	94,940	11	**Al**
		3480	0.21	2.65	89,000	1.3	67,320	1.7	**Li**
JB1_017	187	3365	0.83	2.65	89,000	3.4	95,680	3.2	**Al**
JB1_018	158	3364	0.59	2.65	89,000	2.9	95,930	2.6	**Al**
JB1_019	280	3378	0.52	2.65	89,000	1.4	92,480	1.4	**Al**
		3595	0.09	2.65	89,000	0.3	38,960	0.6	**B**
JB1_020	218	3380	0.73	2.65	89,000	2.6	91,980	2.5	**Al**

Table A1. *Cont.*

Sample	Thickness	Wavenumber	Absorption Integration	Density	ε	H_2O ppm [34]	ε	H_2O ppm [25]	Defect
JB17_001	251	3379	1.09	2.65	89,000	3.3	92,230	3.2	**Al**
JB17_002	189	ND	ND	2.65	89,000	ND	ND	ND	**-**
JB17_003	107	3371	0.21	2.65	89,000	1.5	94,200	0.1	**Al**
		3585	0.01	2.65	89,000	0.1	41,430	0.2	**4H+**
JB17_004	162	3367	22.75	2.65	89,000	107	95,190	100	**Al**
		3480	1.04	2.65	89,000	4.9	67,320	6.5	**Li**
JB17_005	180	3370	0.75	2.65	89,000	3.2	94,450	3.0	**Al**
JB17_006	104	ND	ND	2.65	89,000	ND	ND	ND	**-**
JB17_007	165	3376	1.46	2.65	89,000	6.8	92,970	6.5	**Al**
		3480	0.2	2.65	89,000	0.9	67,320	1.2	**Li**
JB17_008	197	3372	0.23	2.65	89,000	0.9	93,960	0.8	**Al**
JB17_009	237	3371	0.25	2.65	89,000	0.8	94,200	0.8	**Al**
JB17_010	149	ND	ND	2.65	89,000	ND	ND	ND	**-**
JB17_011	224	3368	0.33	2.65	89,000	1.1	94,940	1.1	**Al**
		3595	0.02	2.65	89,000	0.1	38,960	0.2	**B**
JB17_012	110	3377	0.57	2.65	89,000	4.0	92,720	3.8	**Al**
JB17_013	200	ND	ND	2.65	89,000	ND	ND	ND	**-**
JB17_014	207	3365	0.23	2.65	89,000	0.9	95,680	0.8	**Al**
JB17_015	221	3378	1.49	2.65	89,000	5.2	92,480	5.0	**Al**
JB17_016	144	3371	10.55	2.65	89,000	56	94,200	53	**Al**
		3585	0.09	2.65	89,000	0.5	41,430	1.0	**4H+**
JB17_017	162	3363	14.91	2.65	89,000	70	96,170	65	**Al**
		3480	1.58	2.65	89,000	7.4	67,320	9.8	**Li**
		3595	0.06	2.65	89,000	0.3	38,960	0.7	**B**
JB17_018	171	ND	ND	2.65	89,000	ND	ND	ND	**-**
JB17_019	233	3369	12.05	2.65	89,000	40	94,690	37	**Al**
		3480	1.27	2.65	89,000	4.2	67,320	5.5	**Li**
		3595	0.08	2.65	89,000	0.3	38,960	0.6	**B**
JB17_020	177	3370	0.74	2.65	89,000	3.2	94,450	3.0	**Al**
JB23_001	283	3373	0.21	2.65	89,000	0.6	93,700	0.5	**Al**
JB23_002	129	3362	0.3	2.65	89,000	1.8	96,420	1.6	**Al**
JB23_003	206	3373	0.32	2.65	89,000	1.2	93,710	1.1	**Al**
JB23_004	251	3371	0.27	2.65	89,000	0.8	94,200	0.8	**Al**
JB23_005	242	ND	ND	2.65	89,000	ND	ND	ND	**-**
JB23_006	199	ND	ND	2.65	89,000	ND	ND	ND	**-**
JB23_007	279	3372	0.39	2.65	89,000	1.1	93,960	1.0	**Al**
JB23_008	238	3364	0.53	2.65	89,000	1.7	95,930	1.6	**Al**
		3585	0.14	2.65	89,000	0.5	41,430	1.0	**4H+**
JB23_009	186	3367	0.79	2.65	89,000	3.2	95,190	3.0	**Al**
JB23_010	245	3365	0.14	2.65	89,000	0.4	95,680	0.4	**Al**
JB23_011	215	3368	0.15	2.65	89,000	0.5	94,940	0.5	**Al**
JB23_012	167	3373	0.78	2.65	89,000	3.6	93,710	3.4	**Al**
JB23_013	93	ND	ND	2.65	89,000	ND	ND	ND	**-**
JB23_014	179	3369	0.34	2.65	89,000	1.5	94,690	1.4	**Al**
JB23_015	197	3375	0.3	2.65	89,000	1.2	93,220	1.1	**Al**
JB23_016	167	3367	0.41	2.65	89,000	1.9	95,190	1.8	**Al**
		3480	0.07	2.65	89,000	0.3	67,320	0.4	**Li**
JB23_017	206	3374	0.14	2.65	89,000	0.5	93,460	0.5	**Al**
JB23_018	162	3373	0.71	2.65	89,000	3.3	93,710	3.2	**Al**
JB23_019	191	3375	1.09	2.65	89,000	4.4	93,220	4.2	**Al**
		3480	0.03	2.65	89,000	0.1	67,320	0.2	**Li**
JB23_020	202	ND	ND	2.65	89,000	ND	ND	ND	**-**

Table A1. *Cont.*

Sample	Thickness	Wavenumber	Absorption Integration	Density	ε	H_2O ppm [34]	ε	H_2O ppm [25]	Defect
JB26_001	209	3375	0.11	2.65	89,000	0.4	93,220	0.4	**Al**
JB26_002	211	3372	0.94	2.65	89,000	3.4	93,960	3.2	**Al**
		3480	0.02	2.65	89,000	0.1	67,320	0.1	**Li**
JB26_003	197	3372	0.36	2.65	89,000	1.4	93,960	1.3	**Al**
JB26_004	186	3377	1.63	2.65	89,000	6.7	92,720	6.4	**Al**
JB26_005	287	3367	0.3	2.65	89,000	0.8	95,190	0.8	**Al**
JB26_006	233	ND	ND	2.65	89,000	ND	ND	ND	**-**
JB26_007	270	3369	0.47	2.65	89,000	1.3	94,690	1.3	**Al**
JB26_008	223	ND	ND	2.65	89,000	ND	ND	ND	**-**
JB26_009	186	ND	ND	2.65	89,000	ND	ND	ND	**-**
JB26_010	256	ND	ND	2.65	89,000	ND	ND	ND	**-**
JB26_011	252	3376	0.34	2.65	89,000	1.0	92,970	1.0	**Al**
JB26_012	242	3366	0.24	2.65	89,000	0.8	95,430	0.7	**Al**
JB26_013	104	3362	0.29	2.65	89,000	2.1	96,420	2.0	**Al**
JB26_014	181	3374	0.15	2.65	89,000	0.6	93,460	0.6	**Al**
JB26_015	218	3374	0.31	2.65	89,000	1.1	93,460	1.0	**Al**
JB26_016	270	3374	1.41	2.65	89,000	4.0	93,460	3.8	**Al**
JB26_017	235	3367	0.36	2.65	89,000	1.2	95,190	1.1	**Al**
JB26_018	90	3374	0.16	2.65	89,000	1.4	93,460	1.3	**Al**
JB26_019	140	3362	0.24	2.65	89,000	1.3	96,420	1.2	**Al**
JB26_020	163	3370	0.39	2.65	89,000	1.8	94,450	1.7	**Al**
		3585	0.02	2.65	89,000	0.1	41,430	0.2	**4H+**

References

1. Doglioni, C.; Flores, G. *An Introduction to the Italian Geology*; LAMISCO: Potenza, Italy, 1997.
2. Robertson, A.H.F.; Karamata, S. The role of subduction-accretion processes in the tectonic evolution of the Mesozoic Tethys in Serbia. *Tectonophysics* **1994**, *234*, 73–94. [CrossRef]
3. Channell, J.E.T.; Kozur, H.W. How many oceans? Meliata, Vardar, and Pindos oceans in Mesozoic Alpine paleogeography. *Geology* **1997**, *25*, 183–186. [CrossRef]
4. Venturini, S.; Tunis, G. La composizione dei conglomerati cenozoici del Friuli: Dati preliminari. *Stud. Geol. Camerti* **1992**, *2*, 285–295.
5. Ogorelec, B.; Šribar, L.; Buser, S. On lithology and biostratigraphy of Volce Limestone. *Geologija* **1976**, *19*, 126–151.
6. Tunis, G.; Pirini Radrizzani, C. Flyschoid deposits of Goriska Brda (Collio) between Soča (Isonzo) River and Idrija (Iudrio) River —Facies and paleoenvironments. *Geologija* **1987**, *30*, 123–148.
7. Pavlovec, R.; Knez, M.; Drobne, K.; Pavšic, J. Profiles: Košana, Sv. Trojica and Leskovec; the disintegration of the carbonate platform. In *Field Trip Guidebook. ICGP Project 286—Early Paleogene Benthos*; UNESCO: Paris, France, 1991; pp. 69–72.
8. Tunis, G.; Venturini, S. L'Eocene delle Prealpi Carniche, dell'altipiano di Brkini e dell'Istria: Precisazioni biostratigrafiche e paleoambientali. *Nat. Nascosta* **1996**, *13*, 40–49.
9. Magdalenić, Z. Sedimentology of Central Istra Flysch deposits. *Acta Geol. Zagreb* **1972**, *7*, 71–100, (In Croatian with English Summary).
10. Miklavić, B.; Rožić, B. The onset of Maastrichtian basinal sedimentation on Mt. Matajur, NW Slovenia. *RMZ—Mater. Geoenvironment* **2008**, *55*, 199–214.
11. De Min, A.; Rosset, A.; Tunis, G.; Kocmann, C.; Tosone, A.; Lenaz, D. Igneous rock clasts from the Maastrichtian Bovec flysch (Slovenia): Petrology and geodynamic aspects. *Geol. Carpath.* **2007**, *58*, 169–179.
12. Velicogna, M. Zircon Dating and Trace Element Content of Transparent Heavy Minerals in Sandstones from the NE Alps and Outer Dinarides Flysch Basins. Ph.D. Thesis, University of Trieste, Trieste, Italy, 2020.
13. Lenaz, D.; Kamenetsky, V.S.; Crawford, A.J.; Princivalle, F. Melt inclusions in detrital spinel from SE Alps (Italy-Slovenia): A new approach to provenance studies of sedimentary basins. *Contrib. Mineral. Petrol.* **2000**, *139*, 748–758. [CrossRef]
14. Lenaz, D.; Mazzoli, C.; Velicogna, M.; Princivalle, F. Trace and Rare Earth Elements chemistry of detrital garnets in the SE Alps and Outer Dinarides flysch basins: An important tool to better define the source areas of sandstones. *Mar. Pet. Geol.* **2018**, *98*, 653–661. [CrossRef]
15. Lenaz, D.; Princivalle, F. Detrital high pressure—Low temperature minerals in Lower Eocene deep-sea turbidites of the Julian Alps (NE Italy). *Period. Mineral.* **2002**, *71*, 127–135. [CrossRef]
16. Lenaz, D.; Princivalle, F. The crystal chemistry of detrital chromian spinel from the Southeastern Alps and Outer Dinarides: The discrimination of supplies from areas of similar tectonic setting? *Canad. Mineral.* **2005**, *43*, 1305–1314. [CrossRef]

17. De Min, A.; Princivalle, F.; Lenaz, D. Geochemistry of the Late Mesozoic—Early Cenozoic turbidites from the NE part of Adria microplate. *Period. Mineral.* **2014**, *83*, 141–158. [CrossRef]
18. Stalder, R. OH-defects content in detrital quartz grains as an archive for crystallisation conditions. *Sediment. Geol.* **2014**, *307*, 1–6. [CrossRef]
19. Stalder, R.; Konzett, J. OH defects in quartz in the system quartz-albite-water and granite-water between 5 and 25 kbar. *Phys. Chem. Miner.* **2012**, *39*, 817–827. [CrossRef]
20. Stalder, R. OH point defects in quartz—A review. *Eur. J. Mineral.* **2021**, *33*, 145–163. [CrossRef]
21. Bambauer, H.U. Spurenelementgehalte und γ-Farbzentren in Quartzen aus Zerrklüften der Schweizen Alpen. *Schweiz. Miner. Petrogr. Mitt.* **1961**, *41*, 335–369.
22. Kats, A. Hydrogen in alpha quartz. *Philips Res. Rep.* **1962**, *17*, 133–279.
23. Aines, R.D.; Rossman, G.R. Water in minerals? A peak in the infrared. *J. Geophys. Res.* **1984**, *B89*, 4059–4071. [CrossRef]
24. Aines, R.D.; Kirby, S.H.; Rossman, G.R. Hydrogen speciation in synthetic quartz. *Phys. Chem. Miner.* **1984**, *11*, 204–212. [CrossRef]
25. Libowitzky, E.; Rossman, G. An IR absorption calibration for water in minerals. *Am. Mineral.* **1997**, *82*, 1111–1115. [CrossRef]
26. Müller, A.; Koch-Müller, M. Hydrogen speciation and trace elements contents of igneous, hydrothermal and metamorphic quartz from Norway. *Mineral. Mag.* **2009**, *73*, 569–583. [CrossRef]
27. Stalder, R.; Neuser, R.D. OH-defects in detrital quartz grains: Potential for application as tool for provenance analysis ad overview over crustal average. *Sediment. Geol.* **2013**, *294*, 118–126. [CrossRef]
28. Stalder, R.; Potrafke, A.; Billström, K.; Skogby, H.; Meinhold, G.; Gögele, C.; Berberich, T. OH defects in quartz as monitor for igneous, metamorphic, and sedimentary processes. *Am. Mineral.* **2017**, *102*, 1832–1842. [CrossRef]
29. Potrafke, A.; Breiter, K.; Ludwig, T.; Neuser, R.D.; Stalder, R. Variations of OH defects and chemical impurities in natural quartz within igneous bodies. *Phys. Chem. Miner.* **2020**, *47*, 24. [CrossRef]
30. Stalder, R.; von Eynatten, H.; Costamoling, J.; Potrafke, A.; Dunkl, I.; Meinhold, G. OH in detrital quartz grains as tool for provenance analysis: Case studies on various settings from Cambrian to Recent. *Sediment. Geol.* **2019**, *389*, 121–126. [CrossRef]
31. Jaeger, D.; Stalder, R.; Masago, H.; Strasser, M. OH defects in quartz as a provenance tool: Application to fluvial and deep marine sediments from SW Japan. *Sediment. Geol.* **2019**, *338*, 66–80. [CrossRef]
32. Paterson, M.S. The determination of hydroxyl by infrared absorption in quartz, silicate glasses and similar material. *Bull. Minéral.* **1982**, *105*, 20–29. [CrossRef]
33. Rossman, G.R. Analytical methods for measuring water in nominally anhydrous minerals. In *Water in Nominally Anhydrous Minerals*; Reviews in Mineralogy and Geochemistry; Keppler, H., Smyth, J.R., Eds.; Mineralogical Society of America: Boulder, CO, USA, 2006; Volume 62, pp. 1–28. ISBN 0-939950-74-X.
34. Thomas, S.M.; Koch-Müller, M.; Reichart, P.; Rhede, D.; Thomas, R.; Wirth, R.; Matsyuk, S. IR calibrations for water determination in olivine, r-GeO_2, and SiO_2 polymorphs. *Phys. Chem. Miner.* **2009**, *36*, 489–509. [CrossRef]
35. Kamenetsky, V.; Crawford, A.J.; Meffre, S. Factors controlling chemistry of magmatic spinel: An empirical study of associated olivine, Cr-spinel and melt inclusions from primitive rocks. *J. Petrol.* **2001**, *42*, 655–671. [CrossRef]
36. Lenaz, D.; Kamenetsky, V.S.; Princivalle, F. Cr-spinel supply in the Brkini, Istrian and Krk Island flysch basins (Slovenia, Italy and Croatia). *Geol. Mag.* **2003**, *140*, 335–342. [CrossRef]
37. Mange, M.A.; Morton, A.C. Geochemistry of heavy minerals. In *Heavy Minerals in Use*; Developments in Sedimentology; Mange, M.A., Wright, D.T., Eds.; Elsevier: Amsterdam, The Netherlands, 2007; Volume 58, pp. 345–391. [CrossRef]
38. Šarić, K.; Cvetković, V.; Romer, R.L.; Christofides, G.; Koroneos, A. Granitoids associated with East Vardar ophiolites (Serbia, F.Y.R. of Macedonia and northern Greece): Origin, evolution and geodynamic significance inferred from major and trace element data and Sr-Nd-Pb isotopes. *Lithos* **2009**, *108*, 131–150. [CrossRef]
39. Lawrence, S.R.; Tari-Kovačić, V.; Gjukić, B. Geological evolution model of the Dinarides. *Nafta* **1995**, *46*, 103–113.
40. Breiter, K.; Ďurišová, J.; Dosbaba, M. Chemical signature of quartz from S- and A-type rare-metal granites—A summary. *Ore Geol. Rev.* **2020**, *125*, 103674. [CrossRef]